Inverse Problems and Imaging

doi:10.3934/ipi.2026014

OPTIMIZATION-BASED TRANSIONOSPHERIC SAR AUTOFOCUS WITH SCREEN PROJECTION PRECURSOR

Mikhail Gilman[✉] and Semyon Tsynkov[✉*]

Department of Mathematics, North Carolina State University, Raleigh, NC, 27695, USA

(Communicated by Margaret Cheney)

Abstract. Traditional autofocus algorithms for synthetic aperture radar (SAR) are designed for correcting image distortions caused by uncertainties in the antenna trajectory. These algorithms are not well suited for correcting the distortions due to the ionospheric turbulence in the case of spaceborne SAR. The reason is that in conventional imaging with no turbulence, the phase perturbations of SAR signals that cause the distortions depend only on the antenna position while in the case of propagation through turbulence, for each antenna position, they additionally depend on the target coordinates. The latter dependence cannot be adequately addressed by traditional autofocus.

In our previous work, we have built a variational transionospheric SAR autofocus algorithm that circumvents the deficiencies of conventional techniques. It is applied concurrently with the SAR inversion per se, and demonstrates superior performance for a broad range of imaging scenarios. It also outperforms its nearest alternative, which is a two stage non-variational procedure that involves traditional autofocus preceded by screen projection for approximating the ionospheric effects. Yet, the performance of our optimization-based autofocus is not uniform. For high levels of turbulent fluctuations and clutter, its focusing ability appears not as robust because the corresponding optimization formulation is not convex.

In the current work, we enhance the optimization performance in the non-convex case by carefully selecting the initial guess for gradient descent. We choose it as the outcome of the foregoing two stage screen projection algorithm. This leads to a drastic improvement in the quality of focusing while adding little to the computational cost.

1. **Introduction.** Spaceborne synthetic aperture radars (SAR) are prone to image distortions caused by the Earth's ionosphere. The mechanism of distortions can be traced back to the dispersive propagation of radar signals through the ionospheric plasma, which leads to phase perturbations.

There are two types of image distortions, those due to the background ionosphere, and those due to the ionospheric turbulence. The former can be mitigated efficiently via multiple acquisitions (such as dual-carrier probing) followed by registration that

2020 *Mathematics Subject Classification.* Primary: 78A46, 78M50, 86A22; Secondary: 45Q99, 90C26.

Key words and phrases. Synthetic aperture radar (SAR), ionosphere, turbulence, scintillation phase error (SPE), phase screen, autofocus, optimization, non-convexity, screen projection.

Work supported by the US Air Force Office of Scientific Research (AFOSR) under awards nos. FA9550-23-1-0101 and FA9550-24-1-0172.

*Corresponding author: Semyon Tsynkov.

helps determine the unknown ionospheric parameters needed for adjusting the SAR signal processing algorithm, see [4,20] and [5, Chapter 3]. The latter are more difficult to handle because SAR signals propagating between the antenna and different locations on the target travel through different regions of turbulent plasma and thus acquire different phase perturbations. These turbulence-induced perturbations are often referred to as scintillation phase errors (SPEs). They are stochastic in nature, and the corrections obtained with the help of dual-carrier probing appear insufficient for reducing the corresponding distortions. Moreover, as indicated in the recent review paper [13], the defocusing of SAR images due to scintillation phase errors "remains an intractable issue that has not been well mitigated by autofocus processing."

Mitigation of image distortions caused by the propagation of radar signals through the ionospheric turbulence requires reconstruction and suppression of the actual phase perturbations. The reason conventional autofocus algorithms prove inefficient for correcting the turbulence-induced distortions is that they are originally constructed to correct the distortions due to the uncertainties of the antenna trajectory [2,12,22]. Indeed, these algorithms assume that signal perturbations depend only on the antenna coordinate (i.e., slow time). However, in the case of imaging through turbulence, different signal travel paths to and from a given antenna position lead to different phase perturbations [10, 15].

An autofocus algorithm that specifically takes into account the dependence of turbulence-induced signal perturbations on target coordinates was proposed in our work [10]. It is a variational procedure that derives a correction for SPEs as a solution to a special optimization problem. Yet, it is not a complete data-fitting approach (such as full waveform inversion) because it uses a non-variational SAR imaging functional for reconstructing the unknown ground reflectivity. A parameterized form of the unknown SPE correction is included in this functional so that by varying the parameters, one can achieve the optimal focusing.

To represent the ionosphere in our work [10], we have used a simplified model known as the phase screen, which streamlines the analysis and computations. Error estimates supporting the use of a phase screen can be found in [8], while the phase screen elevation can be chosen with the help of the vertical autofocus algorithm of [7].

The performance of the optimization-based methodology of [10] has been found superior for a variety of computer-simulated SAR imaging scenarios. In [9], we have also compared it against that of a conventional autofocus augmented by preprocessing based on screen projection [14] and observed a consistent advantage in the quality of focusing offered by the optimization-based method. In the recent paper [11], we conducted a statistical analysis of the optimization-based autofocus [10] aimed at corroborating its robustness and identifying limitations across a broad range of factors that affect its performance.

An important conclusion drawn in [11] is that the reduction in the focusing quality of the variational algorithm [10] for high levels of turbulent fluctuations and clutter can be attributed to the lack of optimization robustness. Indeed, the optimization problem introduced in [10] for obtaining the SPE correction is nonconvex. A gradient-based optimizer applied to such a problem may converge to a local rather than global minimum, whereas it is the global minimum that yields the proper ionospheric correction. For higher levels of perturbations, local minima

become more prominent, the convergence of the optimizer deteriorates, and so does the focusing performance.

Non-convex optimization is known to be challenging. There are two ways to tackle this problem. One is to try and modify the objective function so that it would become convex, yet its global minimum will not change. This approach is referred to as convexification, see, e.g., [16, 17]. The other way is to use a special global optimization method. As plain gradient-based methods are not well suited for non-convex optimization, they need to be modified accordingly. Modifications may include using multiple initial guesses (multi-start) or combining gradient descent with a swarm-based approach. Alternatively, non-gradient global optimization methods can be applied, such as the original particle swarm optimization, genetic algorithms, or simulated annealing. Typically, those methods converge slowly.

Multi-start is a straightforward methodology that involves starting a gradient-based optimizer from multiple different initial guesses, and subsequently choosing the smallest minimum. There is, of course, no guarantee that the overall minimum found this way will be the true global minimum. Yet, multi-start has led to a substantial increase in focusing quality for the optimization-based autofocus [10, 11]. The downside is that the algorithm is computationally expensive, although its parallelization is easy because all gradient searches are completely independent.

Swarm-based gradient descent [18, 21] uses multiple optimization agents, which is similar to multi-start. Unlike in multi-start though, the searches are not independent, and the agents communicate with one another as the algorithm converges. The results of applying the method of [18, 21] to transionospheric SAR autofocus will be reported in a future publication.

From the analysis of multi-start and swarm gradient descent, one can see that the modifications aimed at enhancing the applicability of gradient-based methods to global optimization basically reduce to finding a good initial guess. Indeed, on a difficult non-convex optimization landscape, if the initial guess happens to be sufficiently close to the true global minimum, then a conventional gradient descent is very likely to converge to it. Of course, there are no universal recipes in non-convex optimization for finding an initial guess located close to the global minimum. For example, in multi-start, one merely explores many initial guesses (often chosen randomly) hoping that at least one will prove right. In the current work, we rather pursue a physics-based rationale.

Specifically, we use the two stage screen projection autofocus of [14] as a precursor to our optimization-based procedure. The algorithm of [14] does not require any optimization and is inexpensive numerically. Even though it is not very accurate on its own, it relies on proper physical assumptions and provides a reasonable prediction of the unknown SPE correction. When this prediction is refined by the optimization-based autofocus of [10], the resulting quality of focusing appears very high for a broad range of imaging scenarios. Yet, the cost of implementation still remains comparable to that of a single gradient descent run.

The rest of the paper is organized as follows. In Section 2, we provide a concise description of the optimization-based autofocus. In Section 3, we outline the key components of the screen projection algorithm. In Section 4, we discuss the combined implementation of the two methods where the screen projection method provides an initial guess for optimization. In Section 5, we present the results of numerical simulations. Finally, in Section 6 we summarize our findings and outline the directions for future work.

2. **Optimization-based autofocus.** The ionosphere is a layer of dilute cold plasma that begins at an altitude of approximately 90 km above the surface of the Earth and extends several hundred kilometers upwards, see [5, Chapter 3]. The plasma is turbulent. Its electron number density fluctuates randomly around the mean value that, in turn, behaves non-monotonically with altitude and reaches a maximum at about 300 km. The orbit altitude for most SAR satellites is well above the ionospheric maximum. Therefore, SAR signals traveling between the satellite and the ground propagate through most of the ionosphere and acquire random phase perturbations due to the temporal dispersion of radio waves in the turbulent ionospheric plasma. A key quantity that determines the magnitude of the phase perturbations is the integral of the electron number density along the signal trajectory. Hence, for different trajectories, the perturbations are, generally speaking, different even if the trajectories originate at the same location (a given position of the SAR satellite). It is precisely due to these phase perturbations, referred to as scintillation phase errors (SPEs), that the ionospheric turbulence causes distortions of spaceborne SAR images. Furthermore, it is the dependence of SPEs not only on the SAR antenna coordinate, but the entire signal travel path that makes the resulting image distortions difficult to ameliorate by traditional autofocus processing [13].

In our previous works [5, Chapter 4] and [3], we have shown that the detrimental effect of turbulence-induced ionospheric SPEs on spaceborne SAR imaging is much stronger in the azimuthal direction (along-the-track) than in the range direction (cross-track). Therefore, in the current paper we will only be considering the one-dimensional stripmap SAR imaging in the azimuthal direction, rendered by range compression (see, e.g., [7, Appendix A.1]).

In [8], we also showed that even though the true ionosphere has finite thickness, for the analysis of transionospheric SAR autofocus, a more basic model that relies on a phase screen provides sufficient accuracy. A phase screen is an infinitesimally thin surface located at an intermediate elevation between the ground and the orbit. There is a function defined on the screen, called the screen density. When the signal travel path intersects the screen, the signal instantaneously acquires the phase perturbation equal to the value of the screen density at the point of intersection, as opposed to the gradual accumulation of perturbations as the signal propagates through a finite thickness ionosphere. In the current paper, we will adopt the phase screen approximation because it renders substantial simplifications.

Consider a given range bin parallel to the satellite orbit, with effective backscattering reflectivity $\mu = \mu(z)$ (see [7, Appendix A.1]). The ground reflectivity μ is the primary unknown to be reconstructed by SAR. The range-compressed signal due to ground reflectivity μ received by the radar antenna at the orbit admits the following integral representation [7]:

$$u(x) = \int_{x-L_{\mathrm{SA}}/2}^{x+L_{\mathrm{SA}}/2} e^{\mathrm{i}\frac{\omega_0(x-z)^2}{Rc}} \cdot e^{-\mathrm{i}\Psi(s(x,z))}\mu(z)\,\mathrm{d}z. \tag{1}$$

In formula (1), z and x denote the cross-range (i.e., azimuthal) coordinates at the ground level and orbit level, respectively, L_{SA} is the length of the synthetic aperture, R is the distance from the orbit to the target area on the ground, c is the speed of light, ω_0 is the radar carrier frequency, and Ψ is the phase screen density that represents the SPEs, see Figure 1.

As the source of the SPEs is the ionospheric turbulence, the SPEs are stochastic in their nature. Accordingly, the phase screen density $\Psi = \Psi(s)$ in equation (1) is

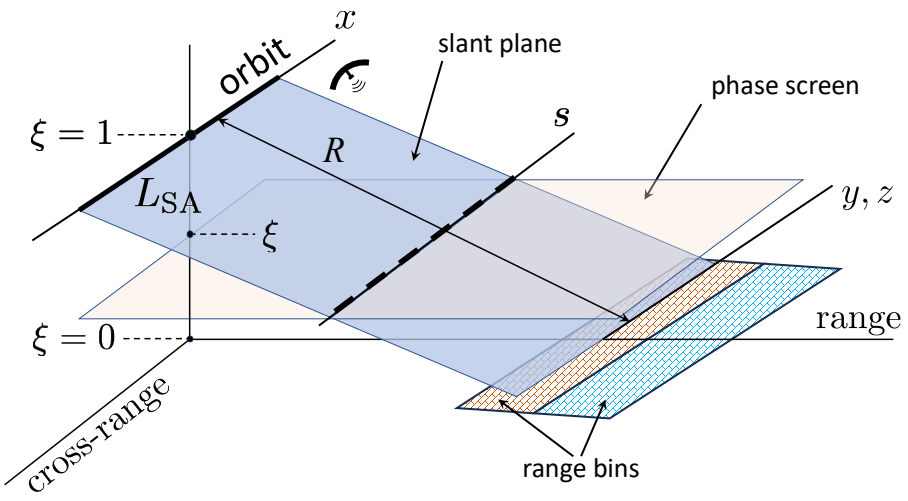

FIGURE 1. Three-dimensional geometry of transionospheric SAR imaging with a phase screen.

considered a realization of a random function of the screen coordinate s. The latter, in turn, is determined by the orbit coordinate x and ground coordinate z:

$$s = s(x, z) = \xi x + (1 - \xi)z, \tag{2}$$

where ξ is the phase screen elevation relative to the orbit height such that $0 \le \xi \le 1$, see Figure 1. In the phase screen model, $\Psi = \Psi(s)$ represents the ionospheric perturbations, while formula (2) accounts for the dependence of these perturbations not only on the antenna coordinate x, but also the target coordinate z. The latter dependence is a key feature of ionospheric phase perturbations that distinguishes them from other perturbations, such as those due to the antenna trajectory uncertainties. In real-life scenarios, the ionospheric phase perturbations Ψ shall be considered unknown. Yet, we will see that to correct the turbulence-induced distortions of SAR images, one needs to know Ψ. To reconstruct the unknown Ψ from the available radar data, one builds the transionospheric autofocus algorithms.[1]

Let us denote by $\Psi^{\mathrm{rec}} = \Psi^{\mathrm{rec}}(s)$ the screen density obtained by reconstruction. It provides a correction for mitigating the distortions due to $\Psi(s)$. The SAR image with correction is written in the integral form (cf. equation (1)), where y denotes the azimuthal coordinate in the image domain (see [10]):

$$\mathcal{I}(y) = \frac{\omega_0}{\pi R c} \int_{y - L_{\mathrm{SA}}/2}^{y + L_{\mathrm{SA}}/2} e^{-\mathrm{i}\frac{\omega_0 (x-y)^2}{Rc}} \cdot e^{\mathrm{i}\Psi^{\mathrm{rec}}(s(x,y))} u(x)\, \mathrm{d}x. \tag{3}$$

The key idea of SAR is to have the image $\mathcal{I}$ of (3) provide an approximation to the ground reflectivity μ in (1). We will see that the constant in front of the integral in (3) is chosen so as to enable this approximation. To analyze the quality of the image $\mathcal{I}$, i.e., how accurately it approximates μ, we substitute the signal $u(x)$ given

[1] They reconstruct a particular realization of the random function Ψ for a given image acquisition.

by (1) into (3):

$$\mathcal{I}(y) = \int_{-\infty}^{\infty} W(y,z)\mu(z)\,\mathrm{d}z. \tag{4}$$

Equation (4) is a very common convolution-type SAR imaging functional [5, Chapter 2], where the imaging kernel $W = W(y,z)$, also referred to as generalized ambiguity function (GAF), is expressed as follows:

$$\begin{gathered} W = \frac{\omega_0}{\pi Rc}\int_{\mathcal{D}} e^{\mathrm{i}\frac{2\omega_0(y-z)(x-(y+z)/2))}{Rc}+\mathrm{i}(\Psi^{\mathrm{rec}}(s(x,y))-\Psi(s(x,z)))}\,\mathrm{d}x, \\ \mathcal{D} = \big\{x \,|\, (|x-z| \le L_{\mathrm{SA}}/2) \cap (|x-y| \le L_{\mathrm{SA}}/2)\big\}. \end{gathered} \tag{5}$$

Formulae (4)–(5) are useful in that they allow one to distinguish between two contributions to the image $\mathcal{I}$: that of the imaging system and ionosphere rendered through W, and that of the ground reflectivity μ. In particular, for a point scatterer $\mu(z) = \delta(z-z_0)$, the image $\mathcal{I}(y)$ coincides with the kernel $W(y,z_0)$, which reduces the analysis of $\mathcal{I}$ to that of W.

If the GAF W is equal to a δ-function, $W(y-z) = \delta(y-z)$, then formula (4) would yield $\mathcal{I} = \mu$. This situation, however, can never be achieved in practice. Even in the ideal case with no ionosphere, $\Psi = \Psi^{\mathrm{rec}} \equiv 0$, the GAF (5) is given by

$$W(y,z) \approx \frac{1}{\Delta_{\mathrm{A}}}\operatorname{sinc}\left(\frac{\pi(y-z)}{\Delta_{\mathrm{A}}}\right), \quad \text{where} \quad \operatorname{sinc}\zeta \stackrel{\mathrm{def}}{=} \frac{\sin\zeta}{\zeta} \quad \text{and} \quad \Delta_{\mathrm{A}} = \frac{\pi Rc}{\omega_0 L_{\mathrm{SA}}}. \tag{6}$$

Formula (6) introduces the well-known sinc kernel that is encountered very often in SAR analyses [5, Chapter 2]. The semi-width of the main lobe of the sinc in (6) is equal to Δ_{A} and defines the azimuthal resolution of a SAR system. Typically, $L_{\mathrm{SA}} \gg \Delta_{\mathrm{A}}$. As the length of the synthetic array L_{SA} increases while the quantity $\frac{\omega_0}{Rc}$ stays constant, the main lobe of the sinc in (6) becomes narrower, and accordingly, the resolution Δ_{A} becomes finer. Moreover, the height of the main lobe of the kernel W increases, and one can show that the kernel converges to the δ-function in the sense of distributions [6, Section 3.3]:

$$\frac{1}{\Delta_{\mathrm{A}}}\operatorname{sinc}\left(\frac{\pi(y-z)}{\Delta_{\mathrm{A}}}\right) \rightharpoonup \delta(y-z), \quad \text{as} \quad L_{\mathrm{SA}} \to \infty \quad \text{and} \quad \frac{\omega_0}{Rc} = \text{const}. \tag{7}$$

Weak convergence (7) along with representation (4) imply $\mathcal{I} \rightharpoonup \mu$ as $L_{\mathrm{SA}} \to \infty$. It is in this sense that the image $\mathcal{I}$ approximates the ground reflectivity μ. Note also that formula (6) itself is also an approximation, which is accurate for $|y-z| \lesssim \Delta_{\mathrm{A}}$. For $|y-z| \gg \Delta_{\mathrm{A}}$, the first exponent on the right-hand side of (5) is large, and the integrand oscillates rapidly, which makes $|W|$ small. Moreover, for $|y-z| \ge L_{\mathrm{SA}}$, the interval of integration defined in (5) is empty, $\mathcal{D} = \emptyset$, so that $W(y,z) = 0$.

While the sinc kernel (6) represents the ultimate scenario with no distortions, in the case where phase perturbations Ψ are present, the role of the correction Ψ^{rec} is to make the actual kernel (5) as close to the undistorted case (6) as possible. One can see, however, that even if $\Psi^{\mathrm{rec}} = \Psi$, the second exponent under the integral in (5) is, generally speaking, not zero, unless $y = z$:

$$\phi_\Psi \stackrel{\mathrm{def}}{=} \Psi^{\mathrm{rec}}(s(x,y)) - \Psi(s(x,z)) = \Psi(s(x,y)) - \Psi(s(x,z)) \neq 0. \tag{8}$$

Hence, even the most accurate phase reconstruction, $\Psi^{\mathrm{rec}} = \Psi$, would still leave some residual ionospheric distortions in the resulting SAR image. In [10], we have

derived an estimate for $|\Psi'(s)|$ and shown that the residual distortions are small. Namely, for a sufficiently smooth $\Psi^{\rm rec} = \Psi$, one has

$$|\phi_\Psi| \sim (1-\xi)\frac{\|\Psi\|}{L_\Psi}\Delta_{\rm A}, \tag{9}$$

where $L_\Psi \gg \Delta_{\rm A}$ is the characteristic spatial scale of ionospheric turbulence. Therefore, the second exponent ϕ_Ψ under the integral in (5) can be neglected even if the magnitude of perturbations $\|\Psi\|$ is not small. Henceforth, we will refer to the case $\Psi^{\rm rec} = \Psi$ as that of the perfect (or ideal) phase error reconstruction. As the true phase error Ψ is not known in practical settings, a transionospheric autofocus algorithm shall be designed so as to provide its best possible approximation $\Psi^{\rm rec}$ using the available SAR data. Moreover, in practice one cannot judge the accuracy of approximation of Ψ by $\Psi^{\rm rec}$ directly. Therefore, the performance of transionospheric autofocus shall be evaluated based on the quality of image focusing.

The optimization-based autofocus that we introduced in [10] employs a parametric representation of the screen density function in the form of a truncated trigonometric series:

$$\Psi(s) = \Re\sum_{n=1}^{N} a_n e^{{\rm i}k_n s + {\rm i}\varphi_n} = \sum_{n=1}^{N}\big(p_n\cos(k_n s) + q_n\sin(k_n s)\big), \tag{10}$$

where $a_n > 0$, $k_n > 0$, φ_n, p_n, and q_n are real. Formula (10) is a mathematical model for SPEs that involves various spatial scales defined by k_n, which is typical for turbulence. In our numerical simulations (see Section 5), formula (10) yields a set of computer-generated data for building and testing the autofocus algorithm. Specifically, in Section 5, the phases φ_n are sampled from a uniform distribution over $[0, 2\pi)^N$, whereas other parameters of Ψ are assumed deterministic. Alternative distributions of φ_n can also be considered.

The autofocus algorithm itself requires no knowledge of Ψ. It uses a variational approach to reconstruct the screen density $\Psi^{\rm rec}$ in the form similar to (10):

$$\Psi^{\rm rec}(s) = \sum_{n=1}^{N^{\rm rec}}\big(p_n^{\rm rec}\cos(k_n^{\rm rec} s) + q_n^{\rm rec}\sin(k_n^{\rm rec} s)\big). \tag{11}$$

In doing so, the signal $u(x)$ given by (1) is taken as input, and optimization is employed to derive the amplitudes $p_n^{\rm rec}$ and $q_n^{\rm rec}$ of the reconstruction density, whereas the frequencies $k_n^{\rm rec}$ and number of terms $N^{\rm rec}$ in (11) are specified ahead of time. They may or may not coincide with the frequencies k_n and number N, respectively, in equation (10), see [10] and Section 5.

The ground reflectivity μ in equation (1) is taken as a finite set of distinct point scatterers with added clutter:[2]

$$\mu(z) = \sum_{m=1}^{M} b_m\delta(z - z_m) + \mu_{\rm clutter}(z), \tag{12}$$

where $\mu_{\rm clutter}(z)$ is a δ-correlated complex-valued Gaussian random process (white noise). While equation (12) represents a fairly specific, rather than general, form of ground reflectivity, we note that the requirement of having bright point scatterers in the imaged scene is most common for the development of SAR autofocus algorithms.

For computer implementation, the integrals (1) and (3) are approximated by quadrature formulae on a uniform discretization grid. Let h denote the grid size,

[2]Clutter makes SAR images visually rough, an effect called *speckle*.

$h = L_{\mathrm{SA}}/J$, where $J > 0$ is an even integer. The nodes of the grid are defined as follows: $x_i = ih$, $i = 0, \pm 1, \pm 2, \dots$ and $z_j = jh$, $j = 0, \pm 1, \pm 2, \dots$ The integral (1) can be discretized using the rectangle rule:

$$u_i = h \sum_{j=i-J/2+1}^{i+J/2} e^{\mathrm{i}\frac{\omega_0 (x_i - z_j)^2}{Rc}} \cdot e^{-\mathrm{i}\Psi(s(x_i, z_j))} \mu_j. \tag{13}$$

If the integrand on the right-hand side of (1) were sufficiently smooth (continuously differentiable), then for $\mu_j = \mu(z_j)$ the quantity u_i on the left-hand side of (13) would approximate $u(x_i)$ with first-order accuracy with respect to h, see, e.g., [19, Section 4.1]. However, the ground reflectivity (12) is anything but smooth (it is a distribution). Therefore, to use formula (13), we first need to properly define μ_j, i.e., build a counterpart of $\mu(z)$ on the grid. For each δ-function in (12), we assume with no loss of generality that its location coincides with one of the grid nodes. Then, we introduce the following discrete equivalent of a δ-function:

$$\delta(z - z_m) \mapsto \delta_j^m = \begin{cases} \frac{1}{h}, & z_j = z_m, \\ 0, & \text{otherwise.} \end{cases} \tag{14}$$

For the clutter $\mu_{\mathrm{clutter}}(z)$, we recall that it is the derivative of a Brownian motion in the sense of distributions (see [1, Chapter 3]). Hence, we can define $\mu_{\mathrm{clutter},\,j}$ as follows:

$$\mu_{\mathrm{clutter},\,j} = \left(\frac{\omega_0}{Rc}\right)^{1/4} \frac{a_{\mathrm{clutter}}}{\sqrt{2h}} n_{\mathrm{clutter},\,j}, \tag{15}$$

where $n_{\mathrm{clutter},\,j}$ is a complex-valued grid function with real and imaginary parts composed of independent standard Gaussian random variables (zero mean and unit variance). The amplitude a_{clutter} in (15) characterizes the clutter intensity, the constant $\left(\frac{\omega_0}{Rc}\right)^{1/4}$ is introduced to adjust the units so that a_{clutter} can be considered dimensionless (see equation (17)), and the denominator $\sqrt{2h}$ accounts for scaling. Recall that in the continuous setting, the Brownian motion, which can be thought of as integral of $\mu(z)$, has standard deviation proportional to the square root of the distance:

$$\sigma\left(\int_0^{L_{\mathrm{SA}}} \mu_{\mathrm{clutter}}(z)\mathrm{d}z\right) \propto \sqrt{L_{\mathrm{SA}}}.$$

Accordingly, for the discretization (15), we have (taking $i = J/2$ with no loss of generality)

$$\begin{aligned} \sigma\Big(h \sum_{j=1}^{J} \mu_{\mathrm{clutter},\,j}\Big) &= \left(\frac{\omega_0}{Rc}\right)^{1/4} \frac{a_{\mathrm{clutter}} h}{\sqrt{2h}} \sigma\Big(\sum_{j=1}^{J} n_{\mathrm{clutter},\,j}\Big) \\ &= \left(\frac{\omega_0}{Rc}\right)^{1/4} a_{\mathrm{clutter}} \sqrt{\frac{h}{2}} \sqrt{2J} = \left(\frac{\omega_0}{Rc}\right)^{1/4} a_{\mathrm{clutter}} \sqrt{L_{\mathrm{SA}}}. \end{aligned} \tag{16}$$

Altogether, the discretized ground reflectivity is given by (cf. equation (12))

$$\mu_j = \sum_{m=1}^{M} b_m \delta_j^m + \mu_{\mathrm{clutter},\,j}, \tag{17}$$

where the individual terms on the right-hand side of (17) correspond to equations (14) and (15). Once substituted into the right-hand of (13), it yields the discrete

radar signal on the grid. For generating the image, the latter is supplemented with additive noise $u_{\mathrm{noise},i}$:

$$u_{\mathrm{noise},\,i} = \frac{a_{\mathrm{noise}}}{\sqrt{2}} \max_i |u_i| n_{\mathrm{noise},\,i}, \tag{18}$$

where $n_{\mathrm{noise},\,i}$ is another instance of the discrete complex-valued Gaussian white noise with zero mean and unit variance. The values of a_{clutter} and a_{noise} are parameters of the model. In the simulations of Section 5, these parameters are varied within a broad range.

A discrete counterpart to continuous image (3) subject to clutter and noise is given by the quadrature formula similar to (13):

$$\mathcal{I}_l = \frac{\omega_0}{\pi Rc} h \sum_{i=l-J/2+1}^{l+J/2} e^{-\mathrm{i}\frac{\omega_0 (x_i - y_l)^2}{Rc}} \cdot e^{\mathrm{i}\Psi^{\mathrm{rec}}(s(x_i,y_l))} (u_i + u_{\mathrm{noise},\,i}), \tag{19}$$

where $y_l = lh$, $l = 0, \pm 1, \pm 2, \ldots$ Note that for the actual implementation, we cannot consider the full unbounded ranges for the indices i, j, and l in formulae (13) and (19). If we assume that the discrete ground reflectivity μ_j is defined on a finite grid interval $J_{\min} \leqslant j \leqslant J_{\max}$, then the signal u_i given by (13) is defined on a smaller grid interval $J_{\min} + J/2 \leqslant i \leqslant J_{\max} - J/2$, and, accordingly, the image $\mathcal{I}_l$ given by (19) is defined on an even smaller interval $J_{\min} + J \leqslant l \leqslant J_{\max} - J$.

For the SAR antenna signal u_i of (13) and imaging functional (19), the variational autofocus algorithm of [10] yields the reconstruction screen density Ψ^{rec}. Since the true perturbation Ψ is unknown, no direct data fitting is possible. Instead, we introduce a cost function $\mathrm{Cost} = \mathrm{Cost}[\mathcal{I}, \Psi^{\mathrm{rec}}]$ that would emphasize the desired features of the image and define Ψ^{rec} as the screen density that delivers a minimum to this cost function. For the target with dominant point scatterers, see formulae (12) and (17), the unperturbed image ($\Psi = \Psi^{\mathrm{rec}} = 0$) will have prominent sinc-shaped peaks. When perturbations $\Psi \neq 0$ are present, the correction Ψ^{rec} should aim at having the peak structure of the image reproduced as close as possible. Therefore, we introduce a sharpness enhancing cost function:

$$\mathrm{Cost}[\mathcal{I}, \Psi^{\mathrm{rec}}] = -\frac{h}{L_{\mathrm{SA}}} \sum_{l=J_{\min}+J}^{J_{\max}-J} |\mathcal{I}_l(\Psi^{\mathrm{rec}})|^4 + \zeta \frac{\omega_0}{Rc} \sum_{n=1}^{N^{\mathrm{rec}}} k_n^2 \big((p_n^{\mathrm{rec}})^2 + (q_n^{\mathrm{rec}})^2\big), \tag{20}$$

where $h/L_{\mathrm{SA}} = 1/J$, the grid values $\mathcal{I}_l = \mathcal{I}_l(\Psi^{\mathrm{rec}})$ are defined by formula (19), and the control variables for minimization are the Fourier coefficients p_n^{rec} and q_n^{rec}, see equation (11). The first sum on the right-hand side of (20) is the negative of the ℓ_4 norm of $\mathcal{I}$ raised to fourth power, while the second sum is a regularization term (penalty) proportional to $\|(\Psi^{\mathrm{rec}})'\|_2^2$. The ℓ_4 term in (20) is known to amplify the sharpness of the image (see [9, 10] and the references therein). The penalty term (second sum in (20)) promotes the decrease of the Fourier amplitudes for higher n, similar to the classical considerations for isotropic turbulence (the Kolmogorov cascade). The coefficient $\frac{\omega_0}{Rc}$ in front of the penalty term in equation (20) is needed to adjust the units. The best penalty weight ζ is determined experimentally when running the optimization algorithm, see Section 5. An extensive discussion about the choice of the cost function (20) can be found in [10, Section 3.2].

To derive Ψ^{rec}, the cost function (20) shall be minimized by varying p_n^{rec} and q_n^{rec}. The quality of minimization determines the autofocus performance. The latter, in turn, is judged by the quality of image focusing, i.e., how well-defined the peaks in the image $\mathcal{I}$ are that are due to the point scatterers in the ground reflectivity μ.

One can evaluate the focusing quality directly because the image (19) is obtained synchronously with minimization of the cost function (20). In the framework of the mathematical model, one can also compare $\Psi^{\rm rec}$ with the original Ψ (see Section 5), but in a practical setting that would not be possible.

Minimization of the cost function (20) is not a trivial task. The main difficulty is that this cost function is non-convex. It may have multiple local minima, and a typical gradient-based optimizer with a given initial guess (often, $p_n^{\rm rec} = q_n^{\rm rec} = 0$) may converge to a local minimum rather than the desired global minimum. That will degrade the quality of focusing. In our previous work [9–11], we have run an extensive series of numerical simulations aimed at quantifying the performance of optimization-based autofocus for various imaging regimes. In [9, 10], we employed an interior-point optimization method implemented via the MATLAB function `fmincon`, whereas in [11] we used the Broyden-Fletcher-Goldfarb-Shanno (BFGS) quasi-Newton method. To assess the quality of image focusing, we utilized three popular metrics of peak sharpness: full width at half magnitude (FWHM), integrated sidelobe ratio (ISLR), and peak height. In [11], we also employed the normalized cross-correlation (NCC) as an image quality metric; computing the NCC requires knowing the image $\mathcal{I}$ in the case of an ideal reconstruction $\Psi^{\rm rec} = \Psi$. Our findings are as follows (see [9–11] for detail).

For moderate levels of ionospheric perturbations and clutter, the gradient-based methods still converge well, which translates into the high quality of focusing. Specifically, for $\|\Psi\|_2 \leqslant 0.8\pi$ and $a_{\rm clutter} \leqslant 0.05$,[3] the peaks in the image obtained by minimizing the cost function (20) with the help of `fmincon` or BFGS and using the resulting $\Psi^{\rm rec}$ in (19) are as well-defined as those in the case of the ideal reconstruction, where $\Psi^{\rm rec} = \Psi$ is substituted into (19).

For high levels of ionospheric perturbations and/or clutter, the convergence of the foregoing gradient-based optimizers is not as robust because of the local minima of $\mathrm{Cost}[\mathcal{I}, \Psi^{\rm rec}]$. This results in higher percentages of defocused images, with peaks not nearly as sharp as the corresponding sinc shapes. To address this issue, we proposed to use multi-start in [10], and further studied its effectiveness in [11]. In multi-start, one initializes the optimizer many times within the domain of the search variables. On an elaborate non-convex optimization landscape, each initial guess yields its own minimum via gradient descent. The expectation is that at least one of those minima will be the true global minimum (or sufficiently close to the true global minimum). There is, of course, no guarantee that this will indeed be the case. But, in practice, the multi-start approach proved efficient, leading to an average increase of the focusing peak height by 10%, and decrease in the value of the cost function by 20%. The potential concern about multi-start is its computational cost, as many gradient searches need to be performed for obtaining one focused image. This concern can be partially alleviated by parallel implementation because all the searches are independent. In [11], we ran the algorithm on a Dell PowerEdge R960 server with four Intel Xeon Platinum 8468H 48-core four-way CPUs, and performed 384 gradient searches simultaneously. As, however, the robustness of multi-start clearly depends on the "density" of initial guesses in the space of optimization

[3] The first of these values approximates the RMS of the phase error in (3), whereas the second does the same for the height of the clutter "floor" relative to that of the isolated peaks, see (15) and Figure 2. The relations between the parameters $\|\Psi\|_2$ and $a_{\rm clutter}$ and some commonly used practical measures that characterize the ionospheric turbulence and clutter are discussed in our works [10, Appendix A] and [11].

variables, for spaces of higher dimensions having a sufficient number of initial guesses could lead to a high computational cost, even for large-scale parallel platforms.

Yet, the observation per se that multi-start helps improve the focusing capacity of the algorithm suggests that having a good initial guess (i.e., an initial guess sufficiently close to the global minimum) is of key importance for the performance of gradient-based optimizers in the non-convex case. Multi-start on its own does not offer any recipes for finding such an initial guess though; it merely tries many independent initial guesses (selected randomly), and subsequently chooses the best result. Therefore, it certainly makes sense to look for more specific, guided strategies for finding the appropriate initial guesses. The main idea of this work is to propose such a strategy based on the relevant physics (see Sections 3–5).

3. **Screen projection autofocus.** An algorithm for transionospheric SAR autofocus was recently proposed in [14] that does not require optimization. It is a two-stage procedure that replaces the SAR reconstruction formula (3) with the following two formulae in succession (see also [9]):

$$p(s) = \frac{1}{\eta L_{\mathrm{SA}}} \int_{s-\eta L_{\mathrm{SA}}/2}^{s+\eta L_{\mathrm{SA}}/2} e^{-\mathrm{i}\frac{\omega_0 (x-s)^2}{\eta R c}} u(x)\,\mathrm{d}x, \tag{21a}$$

$$\mathcal{I}(y) = \frac{C}{\xi}\frac{\omega_0}{\pi R c} \int_{y-\xi L_{\mathrm{SA}}/2}^{y+\xi L_{\mathrm{SA}}/2} e^{-\mathrm{i}\frac{\omega_0 (y-s)^2}{\xi R c}} e^{\mathrm{i}\Psi^{\mathrm{rec}}(s)} p(s)\,\mathrm{d}s, \tag{21b}$$

where $\eta = 1-\xi$ and $C = \left(\frac{\Delta_{\mathrm{A}}}{\xi\eta L_{\mathrm{SA}}}\right)^{-1/2} e^{\mathrm{i}\frac{\pi}{4}}$. The first stage (21a) does not involve any reconstruction phase at all and is otherwise similar to (3), except that the distances are scaled by a factor of η. Hence, one can think that the operator (21a) projects the data $u(x)$, i.e., the antenna signal, to the screen elevation, see Figure 1. That is why it is referred to as screen projection. One can also interpret $p(s)$ of (21a) as a partially-focused image.

The second stage (21b) is also similar to (3), but the distances are scaled by a factor of ξ, and the operator itself is applied to the partially-focused image $p(s)$ from the previous stage (21a) rather than the true antenna signal $u(x)$ of (1). Therefore, the operator (21b) can be thought of as a SAR imaging operator applied to the data $p(s)$ defined at the screen elevation (rather than orbit elevation) and augmented with the phase correction term $\Psi^{\mathrm{rec}}(s)$.

We analyzed the two-stage SAR reconstruction (21) in [9]. For a single point scatterer in the imaged scene, $\mu(z) = \mu_0\delta(z-z_0)$, and no SPEs, $\Psi = 0$, equation (1) yields

$$u(x) = \mu_0 e^{\mathrm{i}\frac{\omega_0 (x-z_0)^2}{Rc}}, \quad \text{where} \quad |x-z_0| \le L_{\mathrm{SA}}/2.$$

Substituting this expression for $u(x)$ into the right-hand side of (21a), we can write

$$\begin{aligned} p(s) &= \frac{\mu_0}{\eta L_{\mathrm{SA}}} \int_{s-\eta L_{\mathrm{SA}}/2}^{s+\eta L_{\mathrm{SA}}/2} e^{-\mathrm{i}\frac{\omega_0 (x-s)^2}{\eta R c}} \cdot e^{\mathrm{i}\frac{\omega_0 (x-z_0)^2}{Rc}}\,\mathrm{d}x \\ &= \mu_0 \int_{-1/2}^{1/2} e^{\mathrm{i}\frac{\omega_0}{Rc}\left[\tilde{x}^2\eta^2 L_{\mathrm{SA}}^2 + 2\tilde{x}\eta L_{\mathrm{SA}}(s-z_0) + (s-z_0)^2 - \tilde{x}^2\eta L_{\mathrm{SA}}^2\right]}\mathrm{d}\tilde{x} \\ &= \mu_0 e^{\mathrm{i}\frac{\omega_0 (s-z_0)^2}{Rc}} \int_{-1/2}^{1/2} e^{\mathrm{i}\frac{\omega_0 \eta L_{\mathrm{SA}}}{Rc}\left[2\tilde{x}(s-z_0) - \tilde{x}^2\xi L_{\mathrm{SA}}\right]}\mathrm{d}\tilde{x}, \end{aligned}$$

where $\tilde{x} = (x-s)/\eta L_{\mathrm{SA}}$. Then, taking the leading term in the stationary phase expansion of the last integral, we obtain (provided that $|s-z_0| \le \xi L_{\mathrm{SA}}/2$)

$$p(s) \approx \mu_0 \left(\frac{\Delta_{\mathrm{A}}}{\xi\eta L_{\mathrm{SA}}}\right)^{1/2} e^{\mathrm{i}\frac{\omega_0(s-z_0)^2}{\xi Rc} - \mathrm{i}\frac{\pi}{4}}. \tag{22}$$

Substituting the partially-focused image $p(s)$ of (22) into the second stage of the reconstruction operator (21b) with $\Psi^{\mathrm{rec}} = 0$, we obtain [cf. equation (5)]

$$\mathcal{I}(y) = \frac{\mu_0}{\xi}\frac{\omega_0}{\pi Rc}\int_{\mathcal{D}'} e^{-\mathrm{i}\frac{\omega_0(y-s)^2}{\xi Rc}} e^{\mathrm{i}\frac{\omega_0(s-z_0)^2}{\xi Rc}}\,\mathrm{d}s = \frac{\mu_0}{\xi}\frac{\omega_0}{\pi Rc}\int_{\mathcal{D}'} e^{\mathrm{i}\frac{\omega_0}{\xi Rc}2(y-z_0)[s-(y+z_0)/2]}\,\mathrm{d}s,$$
$$\mathcal{D}' = \big\{s \,|\, (|s-z_0| \le \xi L_{\mathrm{SA}}/2) \cap (|s-y| \le \xi L_{\mathrm{SA}}/2)\big\}.$$

The previous integral evaluates to [cf. equation (6)]

$$\mathcal{I}(y) \approx \frac{\mu_0}{\Delta_{\mathrm{A}}}\,\mathrm{sinc}\left(\frac{\pi(y-z_0)}{\Delta_{\mathrm{A}}}\right),$$

which indicates that in the absence of phase perturbations, the image resolution offered by the screen projection algorithm (21) is the same as that of the original algorithm (3). However, when the phase perturbations are present, $\Psi \neq 0$, the residual ionospheric distortions of the two-stage algorithm in the ideal case $\Psi^{\mathrm{rec}} = \Psi$ could still be up to $\xi L_{\mathrm{SA}}/\Delta_{\mathrm{A}}$ times higher than similar distortions of the conventional single-stage SAR reconstruction, see formulae (8)–(9). Thus, even for the perfect reconstruction scenario $\Psi^{\mathrm{rec}} = \Psi$, the compensation of SPEs offered by the two-stage method (21) may be considerably less accurate than that of the standard method (3). The reason is that the screen projection (21a) transforms the data $u(x)$ that includes the phase perturbation $\Psi(s)$ in such a way that subsequent application of $\Psi^{\mathrm{rec}} = \Psi$ in (21b) would no longer provide a precise match (see [9, Appendix A] for detail).

In spite of the data contamination at the first stage (21a), the overall algorithm (21) is relevant from the standpoint of physics, and there is a clear rationale behind partitioning the original SAR imaging operator (3) into the scaled stages (21a)–(21b). Namely, at the second stage (21b), the data $p(s)$ and correction $\Psi^{\mathrm{rec}}(s)$ are defined at the same elevation, the screen elevation ξ, and depend on the same single coordinate, the screen coordinate s. This allows one to obtain the unknown correction $\Psi^{\mathrm{rec}} = \Psi^{\mathrm{rec}}(s)$ with the help of traditional autofocus algorithms because the correction depends on the same single argument s as the data does. The authors of [14] developed their methodology for spotlight SAR, and accordingly used the phase gradient autofocus (PGA) to derive the correction Ψ^{rec}. We are considering the stripmap SAR modality, and as such will be using the phase curvature autofocus (PCA), see [23]. The advantage of PCA is that it requires no optimization.

Consider formula (22) for the unperturbed ($\Psi = 0$) partially-focused image $p(s)$ due to the point scatterer $\mu_0\delta(z-z_0)$ on the ground. Up to a constant factor of $C = \left(\frac{\Delta_{\mathrm{A}}}{\xi\eta L_{\mathrm{SA}}}\right)^{-1/2} e^{\mathrm{i}\frac{\pi}{4}}$, it coincides with the radar signal due to the same scatterer that would have been received by the antenna if it were positioned at the same elevation ξ where $p(s)$ is defined:

$$u_\xi(s) = \int_{s-\xi L_{\mathrm{SA}}/2}^{s+\xi L_{\mathrm{SA}}/2} e^{\mathrm{i}\frac{\omega_0(s-z)^2}{\xi Rc}}\mu_0\delta(z-z_0)\,\mathrm{d}z = \mu_0 e^{\mathrm{i}\frac{\omega_0(s-z_0)^2}{\xi Rc}}. \tag{23}$$

Taking the complex argument (i.e., phase) of the screen projected data $p(s)$ given by (22), or, alternatively, of the signal $u_\xi(s)$ given by (23), and differentiating it

twice, we obtain

$$\frac{d^2}{ds^2}\big(\angle p(s)\big) \approx \frac{d^2}{ds^2}\big(\angle u_\xi(s)\big) = \frac{2\omega_0}{\xi Rc} = \text{const}. \tag{24}$$

When $\Psi \neq 0$, one can easily see that formula (23) transforms into

$$u_\xi(s) = \mu_0 e^{\mathrm{i}\frac{\omega_0(s-z_0)^2}{\xi Rc}} e^{-\mathrm{i}\Psi(s)}, \tag{25}$$

and therefore, instead of the second equality of (24), we have

$$\frac{d^2}{ds^2}\big(\angle u_\xi(s)\big) = \frac{2\omega_0}{\xi Rc} - \frac{d^2\Psi(s)}{ds^2}. \tag{26}$$

Unlike in (24), the right-hand side of (26) is no longer constant.

In the actual imaging setting, one does not have $u_\xi(s)$ because there is no antenna at elevation ξ, but can compute $p(s)$ using formula (21a). While our recent analysis of data contamination in [9] shows that the partially-focused image $p(s)$ in the case $\Psi \neq 0$ will not be exactly the same as $u_\xi(s)$ of (25), the original idea of [14] was to directly extend the analogy between (22) and (23) from the case $\Psi = 0$ to the case $\Psi \neq 0$. Then, equation (26) with $p(s)$ substituted instead of $u_\xi(s)$ can be thought of as the definition of the phase correction

$$\frac{d^2\Psi^{\mathrm{rec}}(s)}{ds^2} = \frac{2\omega_0}{\xi Rc} - \frac{d^2}{ds^2}\big(\angle p(s)\big). \tag{27}$$

To derive the actual $\Psi^{\mathrm{rec}}(s)$, one should integrate the right-hand side of equation (27) twice.

Practical implementation of the screen projection autofocus involves multiple range bins, as shown in Figure 1. This approach is standard and dates back to the development of traditional autofocus methods, such as PGA [12, Section 4.5]. It allows one to average out the contributions of clutter, and noise and also enables iterative refinement of the results [9, 12].

The width of a range bin is on the order of range resolution Δ_{R} of the SAR sensor.[4] Consider K such range bins, each containing one strong point scatterer [cf. equation (17)]:

$$\mu_j^{(k)} = b^{(k)}\delta_j^{m_k} + \mu^{(k)}_{\mathrm{clutter},\,j}, \quad k = 1, \ldots, K, \tag{28}$$

where $b^{(k)}$ and m_k are the intensity and location of the point scatterer in kth bin, respectively, and the background $\mu^{(k)}_{\mathrm{clutter},\,j}$ is defined by formula (15), but the realization of the discrete white noise $n_{\mathrm{clutter},\,j}$ is different for each k. The signal due to kth bin is given by [cf. formula (13)]:

$$u_i^{(k)} = h \sum_{j=i-J/2+1}^{i+J/2} e^{\mathrm{i}\frac{\omega_0(x_i-z_j)^2}{Rc}} \cdot e^{-\mathrm{i}\Psi(s(x_i,z_j))}\mu_j^{(k)}, \tag{29}$$

where $\mu_j^{(k)}$ is defined by (28). Noise $u^{(k)}_{\mathrm{noise},\,i}$ is added to the signal (29) [cf. formula (18)]:

$$u^{(k)}_{\mathrm{noise},\,i} = \frac{a_{\mathrm{noise}}}{\sqrt{2}} \max_i |u_i^{(k)}| n_{\mathrm{noise},\,i}, \tag{30}$$

where, again, the realization of $n_{\mathrm{noise},\,i}$ is different for each k. We emphasize that in equation (29), all signals $u_i^{(k)}$, $k = 1, \ldots, K$, are assumed to be affected by one

[4] $\Delta_{\mathrm{R}} = \frac{\pi c}{B}$, where B is the bandwidth of the SAR interrogating waveform (linear chirp) [5, Chapter 2].

and the same phase perturbation function $\Psi(s(x,z))$ that does not depend on k. To justify this assumption, we notice that the variation of distance in the range direction between neighboring bins is comparable to the bin width, or, equivalently, the range resolution Δ_{R}, see Figure 1. Accordingly, at screen elevation, the variation of distance in the range direction between the intersection points of the rays connecting neighboring bins with the antenna is $\sim (1-\xi)\Delta_{\mathrm{R}}$. The range resolution is typically close to azimuthal resolution, and both are much smaller than the characteristic scale of turbulence $\Delta_{\mathrm{R}} \sim \Delta_{\mathrm{A}} \ll L_\Psi$. Therefore, the screen density that represents the phase perturbations can be assumed to vary insignificantly over K adjacent range bins as long as the following condition holds:

$$K(1-\xi)\Delta_{\mathrm{A}} \ll L_\Psi. \tag{31}$$

Let $\{s_m\}$ be a uniform discretization grid on the screen: $s_m = mh$, $m = 0, \pm1, \pm2, \dots$ For each range bin $k = 1, \dots, K$, we approximate the partially focused image (21a) as follows, where the signal and noise are given by formulae (29), (30), respectively [cf. equation (19)]:

$$p_m^{(k)} = \frac{h}{\eta L_{\mathrm{SA}}} \sum_{i=m-\lceil \eta J/2 \rceil + 1}^{m+\lceil \eta J/2 \rceil} e^{-\mathrm{i}\frac{\omega_0 (x_i - s_m)^2}{\eta R c}} (u_i^{(k)} + u_{\mathrm{noise},\,i}^{(k)}). \tag{32}$$

The second derivative on the right-hand side of (27) is discretized by central difference:

$$\frac{d^2}{ds^2}\big(\angle p^{(k)}(s_m)\big) \approx \frac{\angle p_{m+1}^{(k)} - 2\angle p_m^{(k)} + \angle p_{m-1}^{(k)}}{h^2} = \frac{1}{h^2}\angle\big(p_{m+1}^{(k)} p_{m-1}^{(k)} (\bar{p}_m^{(k)})^2\big),$$

where the overbar denotes complex conjugation. In a multi-bin realization, averaging over bins is implemented prior to taking the complex argument (similar to PGA, [12, eqs. (4.39), (F.13)]):

$$\frac{d^2}{ds^2}\big(\angle p_{\mathrm{overall}}(s_m)\big) \approx \frac{1}{h^2}\angle \sum_k p_{m+1}^{(k)} p_{m-1}^{(k)} (\bar{p}_m^{(k)})^2. \tag{33}$$

On the right-hand side of (33), the summation in k is performed over those bins where the signal at $\{m-1, m, m+1\}$ is sufficiently strong (see [9, Section 6] for detail). Approximation (33) is substituted into the right-hand side of (27):

$$\frac{d^2\Psi^{\mathrm{rec}}(s_m)}{ds^2} = \frac{2\omega_0}{\xi R c} - \frac{d^2}{ds^2}\big(\angle p_{\mathrm{overall}}(s_m)\big). \tag{34}$$

Formula (11) defines $\Psi^{\mathrm{rec}}(s)$ as a trigonometric polynomial. Consequently,

$$\big(\Psi^{\mathrm{rec}}(s)\big)'' = \sum_{n=1}^{N^{\mathrm{rec}}} -(k_n^{\mathrm{rec}})^2\big(p_n^{\mathrm{rec}} \cos(k_n^{\mathrm{rec}} s) + q_n^{\mathrm{rec}} \sin(k_n^{\mathrm{rec}} s)\big). \tag{35}$$

On the other hand, we can compute the trigonometric interpolating polynomial for the function defined by (34) on the grid s_m, see [19, Chapter 3]. Using uniqueness of the trigonometric interpolating polynomial [19, Theorem 3.1], we can then claim that the coefficients of the polynomial that corresponds to (34) coincide with the coefficients of the polynomial (35). This allows us to obtain p_n^{rec} and q_n^{rec}, $n = 1, \dots, N^{\mathrm{rec}}$, and thus reconstruct $\Psi^{\mathrm{rec}}(s)$.

The last step of screen projection is iterative refinement of the reconstruction density $\Psi^{\rm rec}(s)$. Having derived $\Psi^{\rm rec}(s)$ from (34)–(35), we define for all $k = 1, \dots, K$

$$\left[p_m^{(k)}\right]_{\rm next} = \left[p_m^{(k)}\right]_{\rm previous} e^{{\rm i}\Psi^{\rm rec}(s_m)}, \tag{36}$$

substitute $\left[p_m^{(k)}\right]_{\rm next}$ into the right-hand side of equation (33), update $\Psi^{\rm rec}(s)$ via (34)–(35), and continue the iteration (36) until convergence, i.e., until the difference between two consecutive iterates of the reconstruction screen density falls blow a predetermined threshold. Iteration (36) can be thought of as a fixed point iteration for screen projection autofocus.

4. **Combined implementation.** The original screen projection methodology of [14] employs the second stage of the reconstruction functional (21b) for obtaining the image $\mathcal{I}$ after the screen density $\Psi^{\rm rec}(s)$ has been derived. We implemented this approach in our previous work [9] to compare the performance of the screen projection autofocus with that of the optimization-based autofocus.

The idea of the current work is different. We do not need to use the second stage of the reconstruction (21b) at all. Rather, we use the reconstruction density $\Psi^{\rm rec}(s)$ obtained by the screen projection iteration (36) as the initial guess for the optimization-based autofocus.

To enable this combined implementation, we reformulate the optimization-based autofocus so that it can be applied in a multi-bin setting that is required for screen projection. The reformulation is straightforward, given that all the range bins $k = 1, \dots K$ are subject to phase perturbations due to the same density $\Psi = \Psi(s(x,z))$, see equation (29). We replace the single-bin cost function ${\rm Cost}[\mathcal{I}, \Psi^{\rm rec}]$ of (20) with its multi-bin counterpart:

$${\rm Cost}_K[\{\mathcal{I}^{(k)}\}, \Psi^{\rm rec}] = -\frac{h}{KL_{\rm SA}} \sum_{k=1}^{K} \sum_{l=J_{\min}+J}^{J_{\max}-J} |\mathcal{I}_l^{(k)}(\Psi^{\rm rec})|^4 + \varsigma \frac{\omega_0}{Rc} \sum_{n=1}^{N^{\rm rec}} k_n^2 \big((p_n^{\rm rec})^2 + (q_n^{\rm rec})^2\big), \tag{37}$$

where the individual images $\mathcal{I}_l^{(k)}$ are obtained by applying formula (19) to the data $u_i^{(k)} + u_{{\rm noise},\, i}^{(k)}$ given by (29)–(30). The new cost function (37) is minimized using the same gradient-based methodology as we employed in our previous work [9], where the control variables are the coefficients $p_n^{\rm rec}$ and $q_n^{\rm rec}$. The cost function ${\rm Cost}_K[\{\mathcal{I}^{(k)}\}, \Psi^{\rm rec}]$ is, generally speaking, not convex, and, therefore, we do not expect that the gradient-based optimizer started from an arbitrary initial guess (often, $p_n^{\rm rec} = q_n^{\rm rec} = 0$) will always perform well. In fact, we saw in our previous work [9–11] that gradient-based optimizers performed unevenly, where more substantial deterioration occurred in the cases with higher levels of phase perturbations and clutter. As, however, we show in Section 5, initiating the gradient-based search with $\Psi^{\rm rec}(s)$ obtained by screen projection, see formula (36), leads to substantial improvements.

The combined implementation of our autofocus algorithm consists of the following steps:

- **Step 1.** The right-hand side of (34) is calculated using one iteration of the screen projection algorithm as described in Section 3.
- **Step 2.** The trigonometric interpolating polynomial on the grid s_m with the wavenumbers $k_n^{\rm rec}$, $n = 1, \dots, N^{\rm rec}$ is built for the result of Step 1 and substituted into the left-hand side of equation (35). It yields the approximate values of the Fourier amplitudes $p_n^{\rm rec}$ and $q_n^{\rm rec}$ for $n = 1, \dots, N^{\rm rec}$.

- **Step 3.** The approximate Fourier amplitudes $p_n^{\rm rec}$ and $q_n^{\rm rec}$, $n = 1, \dots, N^{\rm rec}$, derived in Step 2 are used to initialize the gradient-based optimization with the cost function (37).
- **Step 4.** The result of optimization in Step 3, i.e., $\{p_n^{\rm rec}, q_n^{\rm rec}\}$ for $n = 1, \dots, N^{\rm rec}$, is substituted into (11) and (3) to obtain the focused image.

5. **Results of simulations.** To demonstrate the performance of the combined algorithm, we conduct a series of numerical simulations for the set of parameters similar to those we used in [9,11]. Specifically, we take $L_{\rm SA} = 100$ and $\Delta_{\rm A} = 1$ (units of length presumed but omitted for brevity). This allows us to "reverse engineer" the quantity $\frac{\omega_0}{Rc}$ that appears repeatedly throughout the derivations (see equation (6)). We also take the relative elevation of the screen $\xi = \frac{1}{2}$, while for the screen density (see equation (10)), we choose $N = N^{\rm rec} = 6$, $k_n = nk_1$, $a_n = \left(\frac{k_1}{k_n}\right)^2 a_1$, and $k_n^{\rm rec} = k_n$.[5] From our earlier work [3], we recall that the most challenging scenario for SAR imaging through ionospheric turbulence corresponds to the scale of turbulence L_Ψ being shorter, but not much shorter, than the synthetic aperture $L_{\rm SA}$. We associate L_Ψ with the longest wavelength in the spectrum of turbulence, $l_{\max} = \frac{2\pi}{k_1}$, and analyze two cases: $\frac{L_{\rm SA}}{l_{\max}} = 1.5$ and $\frac{L_{\rm SA}}{l_{\max}} = 2.8$. For the values of the parameters listed above, the penalty weight in front of the second term in equation (37) is taken equal to $\zeta = 0.7/\pi$ based on the numerical experiments conducted in [9] (using [11], it would have been $\zeta = 0.6/\pi$).

We consider $K = 15$ range bins, each containing a single point scatterer (14) at a random location and clutter (see equation (28)). Then, condition (31) is met for either $\frac{L_{\rm SA}}{l_{\max}} = 1.5$ or $\frac{L_{\rm SA}}{l_{\max}} = 2.8$. The level of clutter $a_{\rm clutter}$ varies in simulations (see equation (15)), while the level of noise $a_{\rm noise}$ (see equation (29)) is set equal to that of the clutter.

We also introduce 30 different realizations of the phase screen density $\Psi(s)$ by taking independent random uniformly distributed on $[0, 2\pi]$ phase shifts φ_n for all values of n in equation (10). The intensity of phase perturbations is quantified by means of the L_2 norm:

$$\|\Psi\|_2 = \Big(\sum_n a_n^2\Big)^{1/2} = a_1\Big(\sum_n \Big(\frac{k_1}{k_n}\Big)^4\Big)^{1/2}.$$

This intensity also varies in simulations. Finally, for conducting the simulations, we take the discretization grid size $h = \frac{\Delta_{\rm A}}{8} = \frac{1}{8}$ and apply parabolic windows under the integrals (1), (3), and (21) and under the respective discrete quadrature formulae. We also perform only one iteration (36), because experimentally we have observed that subsequent iterations do not provide any noticeable improvement.

Figure 2 compares several approaches to transionospheric SAR autofocus for a particular example (i.e., a specific screen and specific bin). One can see that the results with no correction ($\Psi^{\rm rec} = 0$) are not satisfactory, the screen projection on its own performs poorly, and the original optimization-based autofocus initialized at zero does better but is still not perfect, while the optimization-based method initialized by screen projection performs on par with ideal reconstruction (i.e., the case of $\Psi^{\rm rec} = \Psi$ which cannot be realized in practice).

[5] In our earlier work [10], we presented the cases of successful focusing in the scenarios where the wavenumber spectra $\{k_n\}$ and $\{k_n^{\rm rec}\}$ are different.

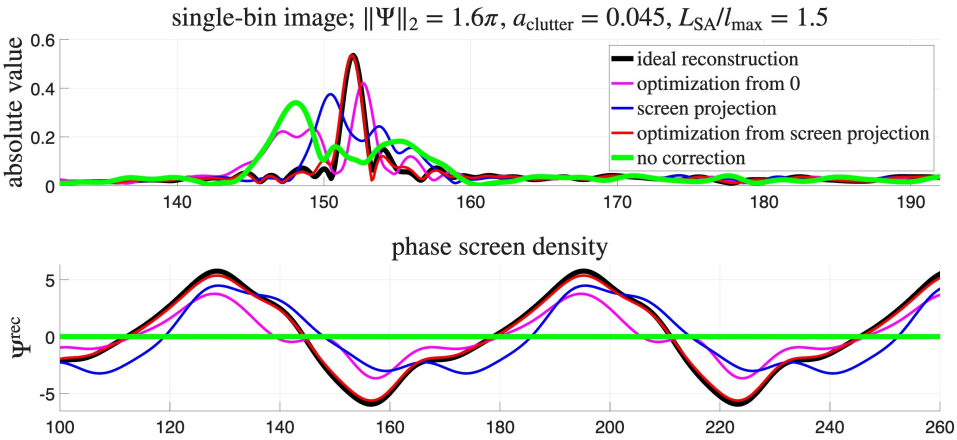

FIGURE 2. Example of reconstruction. Top: single-bin SAR image, bottom: screen density.

A more comprehensive comparison is rendered by incorporating the data across the entire ensemble of targets and screens. In Figure 3, we show the accuracy of reconstruction of the phase screen density for $L_{\text{SA}}/l_{\max} = 1.5$, and two different initializations of the optimization-based autofocus: from zero and from screen projection. Each of the six panels contains 25 colored tiles, where each tile corresponds to the ensemble of 30 realizations of Ψ for the specified values of $\|\Psi\|_2$ and a_{clutter}. We see that initialization from screen projection provides a considerably more accurate reconstruction across the ensemble.

In Figure 4, we show a comparison similar to that shown in Figure 3, but for a shorter scale of ionospheric turbulence: $L_{\text{SA}}/l_{\max} = 2.8$. This is a more challenging scenario from the standpoint of physics, and the autofocus performance deteriorates for either type of initialization. Yet, initialization from screen projection still noticeably outperforms the initialization from zero. In the future, we will investigate ways of further improving the performance in the case of shorter turbulence scales.

The following series of plots compares the quality of focusing for three algorithms: optimization-based autofocus initialized from zero, screen projection autofocus on its own, and the combined algorithm, i.e., optimization-based autofocus initialized from screen projection; all three are compared against ideal reconstruction $\Psi^{\text{rec}} = \Psi$. Similar to Figures 3 and 4, we conduct the comparison for the entire ensemble of screen densities and target reflectivities, and for varying levels of phase perturbations and clutter.

In Figure 5, we present three focusing quality metrics: FWHM, ISLR, and peak height for the optimization-based autofocus initialized from zero in the case of $L_{\text{SA}}/l_{\max} = 1.5$. They are compared with the same metrics for ideal reconstruction. In Figure 6, a similar comparison is conducted for the screen projection autofocus alone, and in Figure 7, for the optimization-based autofocus initialized from screen projection. The optimization-based autofocus initialized from screen projection demonstrates the best performance.

In Figures 8, 9, and 10, we compare the focusing quality of the three autofocus techniques against that for ideal reconstruction in the case of $L_{\text{SA}}/l_{\max} = 2.8$. As

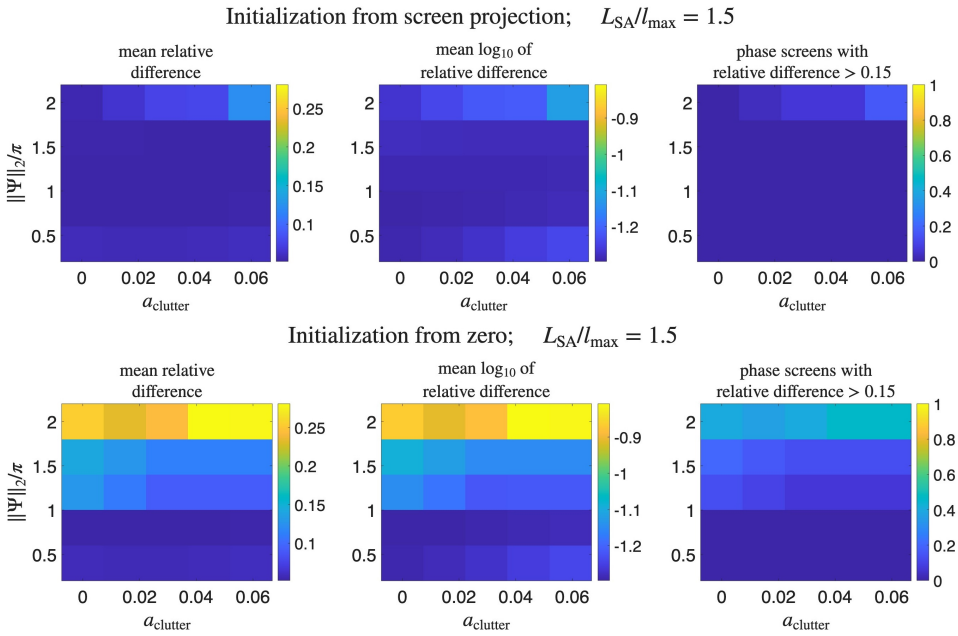

FIGURE 3. Comparative accuracy of reconstruction of the phase screen density for $L_{SA}/l_{max} = 1.5$. Top row: initialization from screen projection; bottom row: initialization from zero. Left column: mean$\left(\frac{\|\Psi^{rec}-\Psi\|_2}{\max\{\|\Psi^{rec}\|_2,\|\Psi\|_2\}}\right)$, center column: mean$\left(\log_{10}\frac{\|\Psi^{rec}-\Psi\|_2}{\max\{\|\Psi^{rec}\|_2,\|\Psi\|_2\}}\right)$, right column: the fraction of phase screens with $\frac{\|\Psi^{rec}-\Psi\|_2}{\max\{\|\Psi^{rec}\|_2,\|\Psi\|_2\}} > 0.15$.

in the case $L_{SA}/l_{max} = 1.5$ (see Figures 5, 6, and 7), the combined algorithm, i.e., optimization-based autofocus initialized from screen projection, shows superior performance compared to the other two methods, although the overall quality for the shorter scale of turbulence ($L_{SA}/l_{max} = 2.8$) is somewhat lower than that for the longer scale of turbulence ($L_{SA}/l_{max} = 1.5$).

6. **Discussion.** Optimization-based transionospheric SAR autofocus developed in [10] and further analyzed and improved in [9, 11] can render high quality focusing, but requires solving a challenging non-convex optimization problem. Multiple local minima that characterize this optimization problem make the application of gradient-based methods not straightforward. This, in turn, reduces robustness of the entire procedure, especially in the case of high levels of ionospheric phase perturbations and clutter.

Previously, we have shown that the performance of gradient-based optimizers strongly depends on the choice of the initial guess. In this work, we introduced a physics-informed strategy for choosing the initial guess for gradient-based autofocus optimization. Specifically, we choose it as the output of the screen projection algorithm that has earlier been proposed in [14] as an enhancement of conventional SAR autofocus methods aimed at adapting them to transionospheric imaging. A key advantage of the screen projection approach is that it is computationally inexpensive

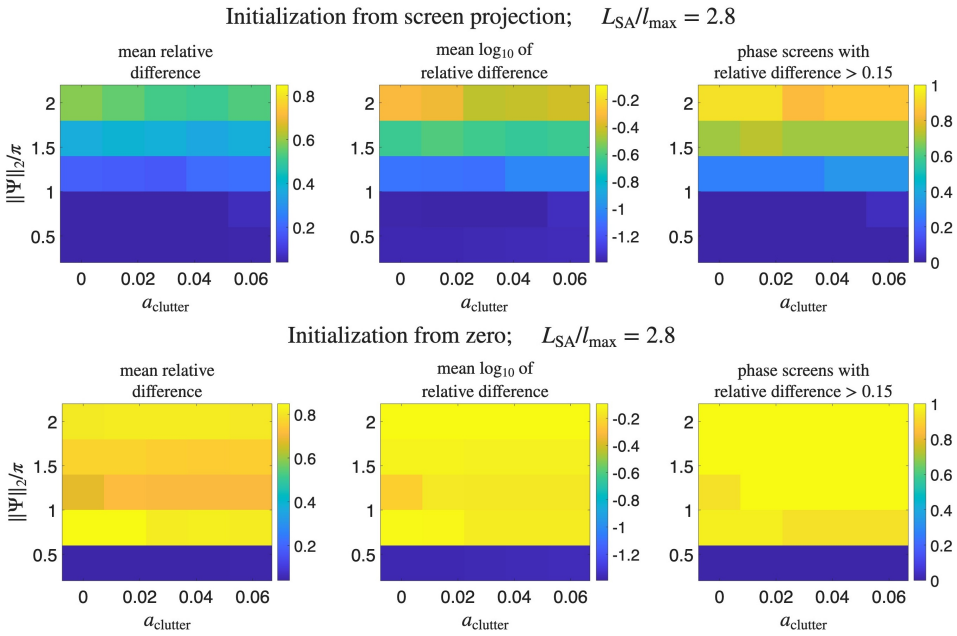

FIGURE 4. Comparative accuracy of reconstruction of the phase screen density for $L_{SA}/l_{max} = 2.8$. Top row: initialization from screen projection; bottom row: initialization from zero. Left column: mean$\left(\frac{\|\Psi^{rec}-\Psi\|_2}{\max\{\|\Psi^{rec}\|_2,\|\Psi\|_2\}}\right)$, center column: mean$\left(\log_{10}\frac{\|\Psi^{rec}-\Psi\|_2}{\max\{\|\Psi^{rec}\|_2,\|\Psi\|_2\}}\right)$, right column: the fraction of phase screens with $\frac{\|\Psi^{rec}-\Psi\|_2}{\max\{\|\Psi^{rec}\|_2,\|\Psi\|_2\}} > 0.15$.

and does not involve a variational component. Using its result as the initial guess for optimization proves very beneficial as it leads to a substantial improvement of the focusing capacity of optimization-based transionospheric SAR autofocus.

The results of numerical simulations presented in Section 5 corroborate the improved performance of the optimization-based SAR autofocus due to taking the screen projection output as initial guess for optimization. However, in the current set of simulations, we considered only a small number of range bins ($K = 15$) that define the performance of the screen projection itself. The reason for the limitation is that the overall width of those bins must be much smaller than the characteristic spatial scale of turbulence, which, in turn, should be shorter than the length of the synthetic array. On the other hand, using more bins for the screen projection may improve the performance even further. To allow for a larger number of range bins still under the turbulence scale, we will need to simulate the scenarios with much longer synthetic arrays. These scenarios are also more realistic, as in the actual spaceborne SAR systems the ratio of the synthetic aperture to azimuthal resolution could be in the thousands. Yet, the corresponding simulations are expected to be computationally more costly, and will be conducted in the future.

Beyond that, we contemplate a number of additional developments. On the side of physics, they may include use of the true Kolmogorov spectrum of turbulence,

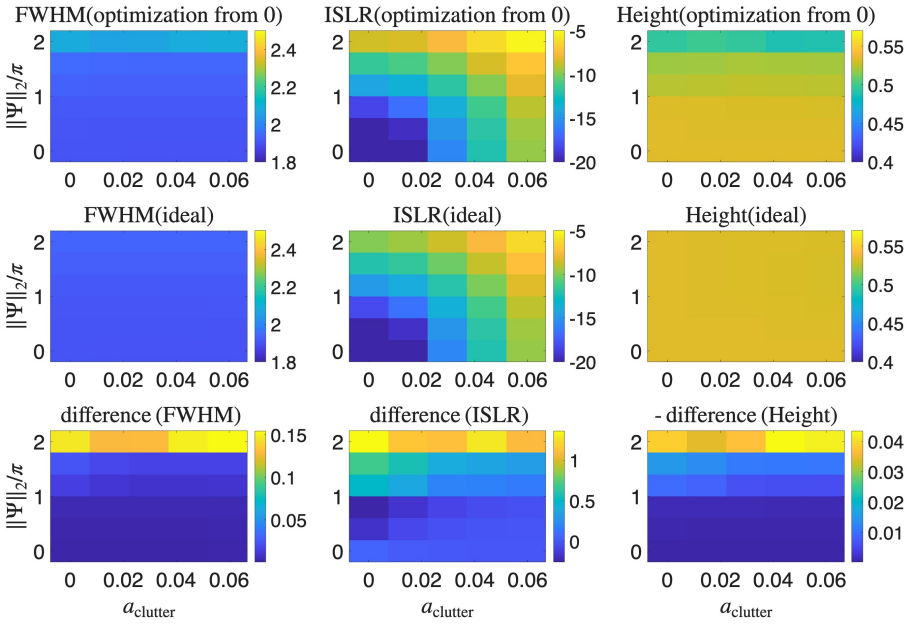

FIGURE 5. Performance of optimization-based autofocus initialized at zero for $L_{\text{SA}}/l_{\max} = 1.5$.

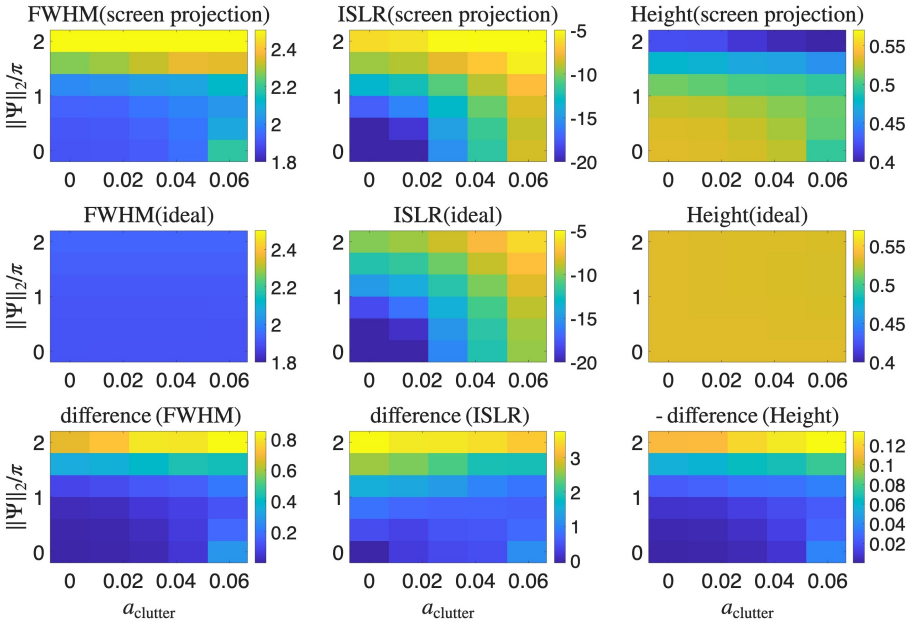

FIGURE 6. Performance of screen projection autofocus for $L_{\text{SA}}/l_{\max} = 1.5$.

construction of a more accurate model of ionosphere based on multiple screens or a layer of plasma of finite thickness, extension from point scatterers to general

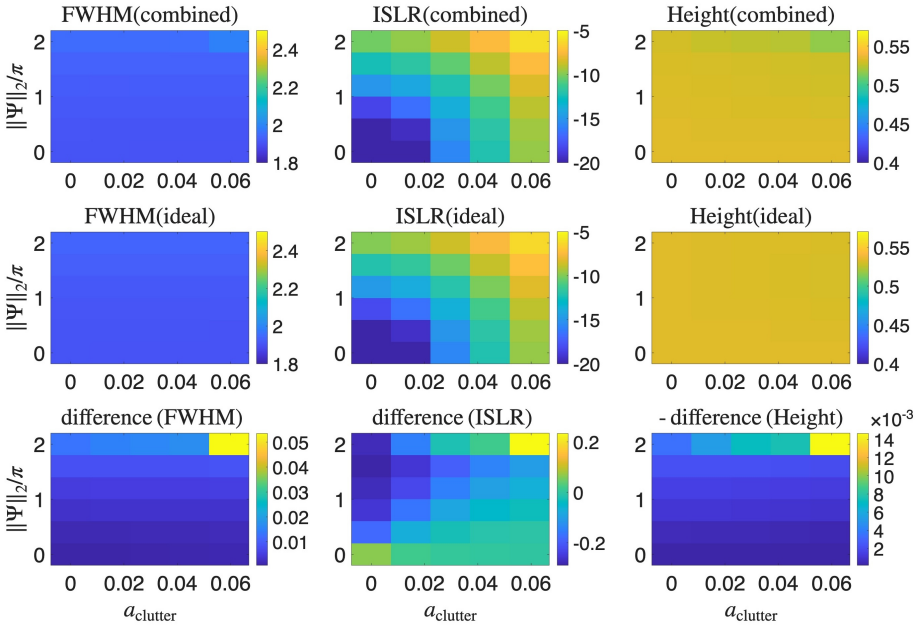

FIGURE 7. Performance of the combined algorithm, i.e., optimization-based autofocus initialized from screen projection, for $L_{\text{SA}}/l_{\max} = 1.5$.

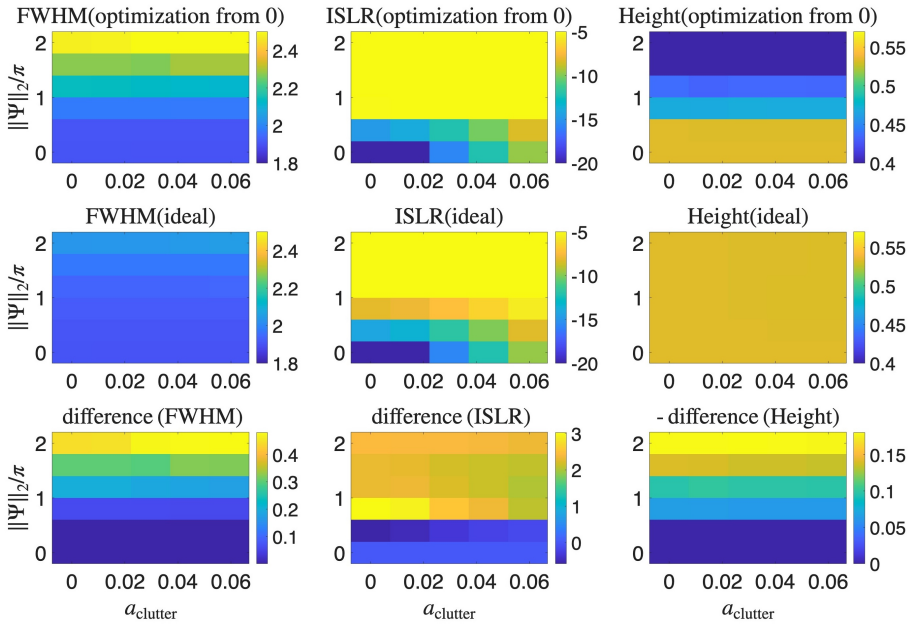

FIGURE 8. Performance of optimization-based autofocus initialized at zero for $L_{\text{SA}}/l_{\max} = 2.8$.

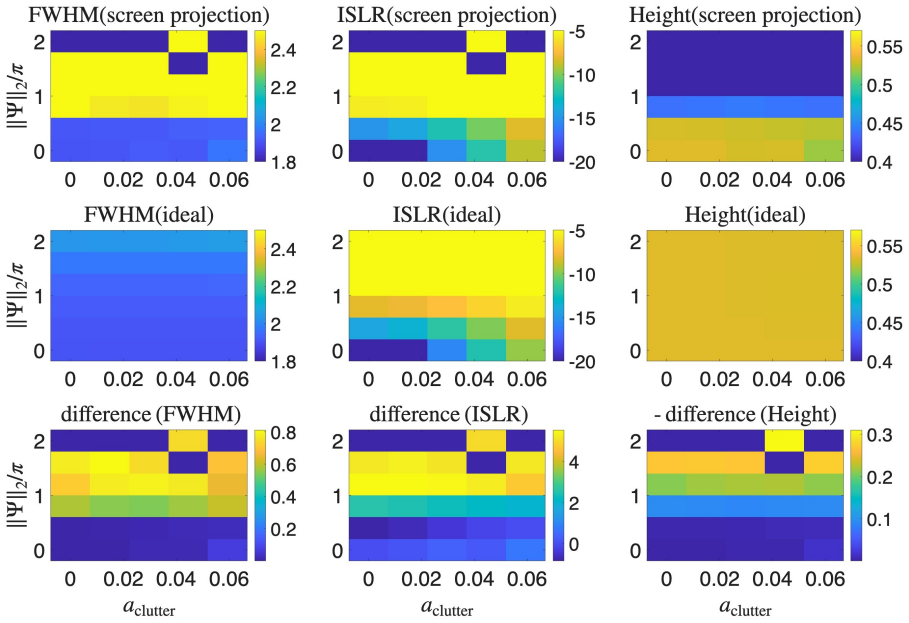

FIGURE 9. Performance of screen projection autofocus for $L_{\text{SA}}/l_{\max} = 2.8$.

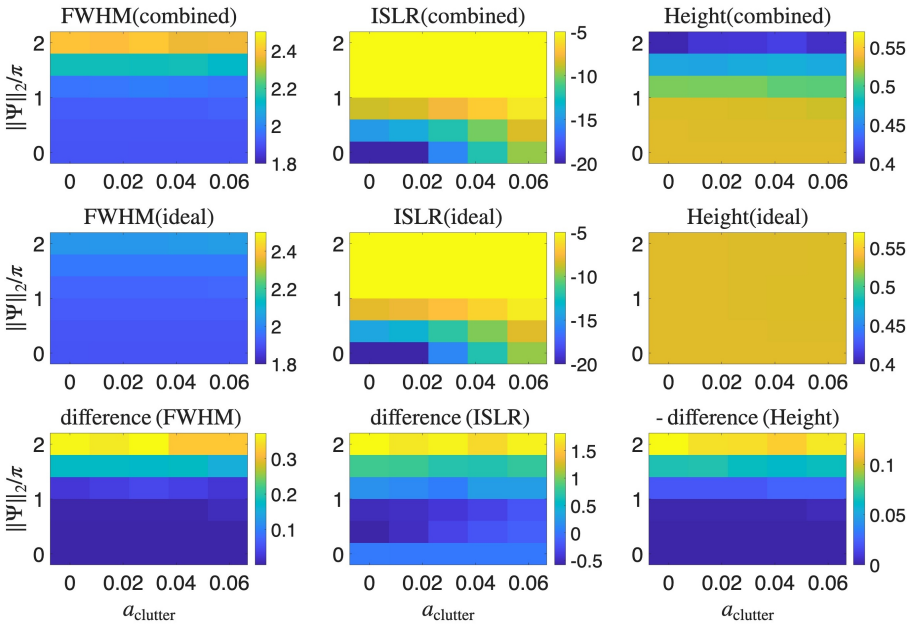

FIGURE 10. Performance of the combined algorithm, i.e., optimization-based autofocus initialized from screen projection, for $L_{\text{SA}}/l_{\max} = 2.8$.

scatterers, and transition from the range compressed formulation to the true two-dimensional SAR images. On the methodological side, we may consider other types of cost functions for optimization, as well as additional criteria for assessing the quality of the image focusing.

Acknowledgment. It is our pleasure to thank Professor M. V. Klibanov of UNC Charlotte for many helpful discussions on the subject of global optimization.

REFERENCES

[1] A. J. Chorin and O. H. Hald, *Stochastic Tools in Mathematics and Science*, Surveys and Tutorials in the Applied Mathematical Sciences, Vol 1. Springer, New York, 2006.

[2] I. G. Cumming and F. H. Wong, *Digital Processing of Synthetic Aperture Radar Data. Algorithms and Implementation*, Artech House, Boston, 2005.

[3] M. Gilman and S. Tsynkov, Mathematical analysis of SAR imaging through a turbulent ionosphere, *Application of Mathematics in Technical and Natural Sciences: 9th International Conference for Promoting the Application of Mathematics in Technical and Natural Sciences — AMiTaNS'17, AIP Conference Proceedings, American Institute of Physics (AIP)*, **1895** (2017), 020003, 23 pp.

[4] M. Gilman, E. Smith and S. Tsynkov, Reduction of ionospheric distortions for spaceborne synthetic aperture radar with the help of image registration, *Inverse Problems*, **29** (2013), 054005, 35 pp.

[5] M. Gilman, E. Smith and S. Tsynkov, *Transionospheric Synthetic Aperture Imaging*, Applied and Numerical Harmonic Analysis, Birkhäuser/Springer, Cham, Switzerland, 2017.

[6] M. Gilman and S. Tsynkov, A mathematical perspective on radar interferometry, *Inverse Problems & Imaging*, **16** (2022), 119-152.

[7] M. Gilman and S. Tsynkov, Vertical autofocus for the phase screen in a turbulent ionosphere, *Inverse Problems*, **39** (2023), 045001, 36 pp.

[8] M. Gilman and S. Tsynkov, Modeling the Earth's ionosphere by a phase screen for the analysis of transionospheric SAR imaging, *IEEE Trans. Geosci. Remote Sens.*, **62** (2024), 2000216, 16 pp.

[9] M. Gilman and S. Tsynkov, Comparative analysis of performance for optimization-based transionospheric SAR autofocus, *Radio Science*, **60** (2025), 2024RS008168.

[10] M. Gilman and S. V. Tsynkov, Transionospheric autofocus for synthetic aperture radar, *SIAM J. Imaging Sci.*, **16** (2023), 2144-2174.

[11] P. Haughey, M. Gilman and S. Tsynkov, Statistical analysis of performance of optimisation-based SAR autofocus, *IET Radar, Sonar & Navigation*, **19** (2025), e70030, https://ietresearch.onlinelibrary.wiley.com/doi/abs/10.1049/rsn2.70030.

[12] C. V. Jakowatz Jr., D. E. Wahl, P. H. Eichel, D. C. Ghiglia and P. A. Thompson, *Spotlight-Mode Synthetic Aperture Radar: A Signal Processing Approach*, Springer, 1996.

[13] Y. Ji, Z. Dong, Y. Zhang, C. Wang, C. Hu and Z. Xu, Transionospheric synthetic aperture radar observation: A comprehensive review, *IEEE Geoscience and Remote Sensing Magazine*, 2-43.

[14] Y. Ji, C. Yu, Q. Zhang, Z. Dong, Y. Zhang and Y. Wang, An ionospheric phase screen projection method of phase gradient autofocus in spaceborne SAR, *IEEE Geoscience and Remote Sensing Letters*, **19** (2022), 1-5.

[15] J. S. Kim, K. P. Papathanassiou, R. Scheiber and S. Quegan, Correcting distortion of polarimetric SAR data induced by ionospheric scintillation, *IEEE Transactions on Geoscience and Remote Sensing*, **53** (2015), 6319-6335.

[16] M. V. Klibanov and O. V. Ioussoupova, Uniform strict convexity of a cost functional for three-dimensional inverse scattering problem, *SIAM J. Math. Anal.*, **26** (1995), 147-179.

[17] M. V. Klibanov and J. Li, *Inverse Problems and Carleman Estimates—Global Uniqueness, Global Convergence and Experimental Data*, Inverse and Ill-posed Problems Series, 63. De Gruyter, Berlin, 2021.

[18] J. Lu, E. Tadmor and A. Zenginoglu, Swarm-based gradient descent method for non-convex optimization, *Commun. Am. Math. Soc.*, **4** (2024), 787-822.

[19] V. S. Ryaben'kii and S. V. Tsynkov, *A Theoretical Introduction to Numerical Analysis*, Chapman & Hall/CRC, Boca Raton, FL, 2007.

[20] E. M. Smith and S. V. Tsynkov, Dual carrier probing for spaceborne SAR imaging, *SIAM J. Imaging Sci.*, **4** (2011), 501-542.
[21] E. Tadmor and A. Zenginoglu, Swarm-based optimization with random descent, *Acta Appl. Math.*, **190** (2024), Paper No. 2, 21 pp.
[22] D. E. Wahl, P. H. Eichel, D. C. Ghiglia and C. V. Jakowatz Jr., Phase gradient autofocus — A robust tool for high resolution SAR phase correction, *IEEE Trans. Aerosp. Electron. Syst.*, **30** (1994), 827-835.
[23] D. E. Wahl, C. V. Jakowatz Jr., P. A. Thompson and D. C. Ghiglia, New approach to strip-map SAR autofocus, *Sixth IEEE Digital Signal Processing Workshop*, (1994), 53-56.

Received for publication October 26, 2025; early access January 21, 2026.